

Imaging with subwavelength resolution by a generalized superlens at infrared wavelengths

B. D. F. Casse,¹ W. T. Lu,¹ R. K. Banyal,¹ Y. J. Huang,¹ S. Selvarasah,² M. R. Dokmeci,²
C. H. Perry,¹ and S. Sridhar^{1,*}

¹Electronic Materials Research Institute and Department of Physics, Northeastern University,
Boston, Massachusetts 02115, USA

²Department of Electrical and Computer Engineering, Northeastern University, Boston, Massachusetts 02115, USA

*Corresponding author: S.Sridhar@neu.edu

Received March 18, 2009; revised May 28, 2009; accepted May 31, 2009;
posted June 8, 2009 (Doc. ID 108873); published June 24, 2009

We demonstrate experimentally negative refraction by a photonic crystal prism and imaging of a point source by a photonic crystal slab at 1.5 μm wavelength. The photonic crystal structures were nanofabricated in a InGaAsP/InP heterostructure platform, and optical characterization was performed using a near-field scanning optical microscope. By designing a suitable lens surface termination, an image spot size of $0.12\lambda^2$ was achieved, demonstrating superlens imaging with subwavelength resolution well below Abbe's diffraction limit ($0.5\lambda^2$). © 2009 Optical Society of America
OCIS codes: 160.1245, 110.3080.

The most celebrated consequence of negative refraction (NR) [1] is the Veselago–Pendry perfect lens [2]. This perfect lens, made of a homogeneous medium, operates at a fixed frequency with $n = \epsilon = \mu = -1$ and can resolve subwavelength geometrical details of an object by amplification of evanescent waves, theoretically with infinite spatial resolution. However, NR media constructed with realistic materials, especially metallic-based metamaterials [3,4], are intrinsically lossy (due to the imaginary part of ϵ and μ), which limits the resolution of the lens [5]. Nevertheless, subwavelength imaging is still possible to some degree with these imperfect lenses, which we henceforth refer to as “superlenses.” The fundamental challenge of dealing with material losses led some researchers to investigate low-loss dielectric photonic crystals (PhCs) as NR media, in which the behavior of a negative-refractive-index homogeneous metamaterial can be emulated [6,7] by appropriately designing the PhC lattice. In the microwave spectral range, both NR and subwavelength resolution imaging have been clearly demonstrated, while in optics only partial concepts of NR have been shown [8–13] mostly with the absence of subwavelength resolution. Notable success has been achieved in constructing the so-called “poor man’s” superlens [2,14], which, however, do not achieve actual focusing of propagating waves, which is required for full imaging.

In this work, we utilize band structure calculations to design and fabricate (i) a negative-index PhC prism and (ii) a flat lens in InGaAsP/InP heterostructure at telecommunication frequencies. Optical experiments were carried out confirming NR by the PhC prism and imaging of a point source by the PhC flat lens. Most importantly, the imaging experiments show that in addition to image formation by propagating waves, reconstruction of evanescent waves (superlensing effect) was also achieved by appropriate modification of the lens surface, leading to a spot size of $0.12\lambda^2$, which is below the diffraction limit ($0.5\lambda^2$).

The fabrication platform consisted of a 400 nm InGaAsP core layer on an InP substrate with a 200 nm InP top cladding layer. The waves are trapped and propagate within the core layer plane with an effective permittivity. At 1.52 μm , the effective permittivity is $\epsilon_{\text{eff}} = 10.44$ for the TE waves, while $\epsilon_{\text{eff}} = 10.34$ for the TM waves. Here, we use $n_{\text{InP}} = 3.17$ and $n_{\text{core}} = 3.35$. The band structure of the quasi-2D PhC is then calculated as a 2D PhC with a constant effective permittivity by employing a standard plane-wave expansion method. The 2D band structure of a square lattice PhC with air holes of 290 nm diameter and a lattice spacing of 470 nm is shown in Fig. 1(a).

We demonstrate NR by a PhC prism created from a square lattice with geometrical dimensions stated above forming a right-angle triangle with sides of equal length of 100 μm . The final structure for optical characterization of the PhC prism includes (i) an array of 5- μm -wide, 0.5-mm-long waveguides with 10- μm -wide trenches on each side, and (ii) an air cavity at the hypotenuse interface of the PhC as shown in Fig. 1(c). IR light at 1.52 μm was coupled into the single-mode ridge waveguide that interconnects the right-angle PhC prism through a single-mode lensed fiber. The out-of-plane radiated light was imaged from above with a high-sensitivity near-IR camera.

The incident light path due to the radiation from the PhC is clearly seen in the IR image shown in Fig. 1(c). To probe the outgoing radiation at the hypotenuse face of the PhC prism–air interface, a 2- μm -deep triangular-shaped air cavity was etched next to the PhC prism. The emerging light inside the air cavity was collected with a 250 nm metallized aperture of a single-mode optical fiber probe of the near-field scanning optical microscope (NSOM).

In the NSOM image shown in Fig. 1(d), the direction of the emerging beam is clearly negative. The refracted beam angle was consistently found to be about $\approx 30^\circ$ for all waveguide inputs. The incidence angle at the second interface is equal to the prism

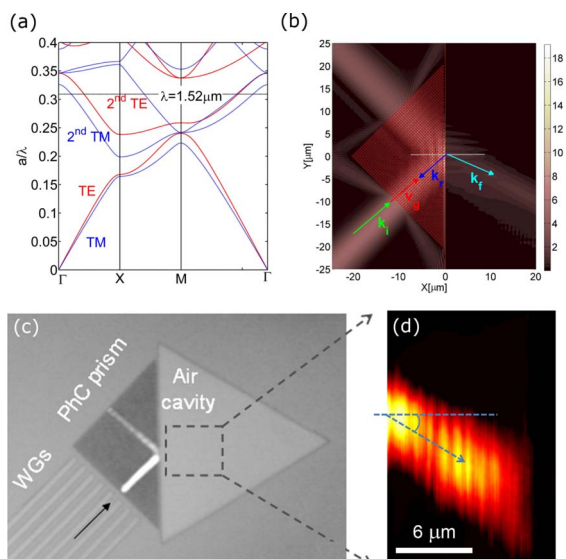


Fig. 1. (Color online) (a) Band structure of a square PhC consisting of air holes with $r/a=0.31$ in $\epsilon_{\text{eff}}=10.44$ for the TE modes (solid curves) and $\epsilon_{\text{eff}}=10.34$ for the TM modes (dashed curves). The horizontal dashed line is at $\lambda=1.52\ \mu\text{m}$ for $a=470\ \text{nm}$. (b) FDTD simulation of TE polarized light beam showing negative refraction at the PhC prism–air interface. The incident beam with \vec{k}_i is in the dense medium with ϵ_{eff} . (c) Image of the right angle PhC prism captured with a $50\times$ long-focal-distance microscope objective. The arrow indicates the direction of input light from the waveguide. The illuminated region inside the PhC prism was imaged with a high-sensitivity near-IR camera, and (d) is a NSOM area scan ($30\ \mu\text{m}\times 30\ \mu\text{m}$) showing the negatively refracted beam in free space (dashed arrow).

wedge angle 45° . The corresponding phase refractive index obtained from Snell's law is approximately $n_p=-0.71$, which closely matches with the band structure calculation of $n_p=-0.67$. The experimental results were further confirmed by 2D finite-difference time-domain (FDTD) simulations. The FDTD simulation of a TE beam with $\lambda=1.52\ \mu\text{m}$ incident on a PhC prism clearly shows NR in Fig. 1(b).

Next, we demonstrate flat lens imaging by the PhC and the superlensing effect by appropriate modification of surface terminations for TE-polarized light. Imaging of a point source is achieved using a PhC flat lens fabricated by patterning a square lattice of air holes on InGaAsP/InP. The PhC flat lens has the same lattice geometrical configuration as the PhC prism used in NR. To facilitate the NSOM measurements, a $10\ \mu\text{m}\times 20\ \mu\text{m}$ rectangular air cavity is etched next to the PhC slab. To avoid overexposing the PhC slab with the electron beam during the fabrication process, a dense medium gap of $\approx 0.7\ \mu\text{m}$ ($0.9\ \mu\text{m}$) is maintained between the first (second) air–PhC interface as shown in Fig. 2. The dense medium gaps can also serve to localize electromagnetic modes (known as surface states) which may be employed to achieve amplification of evanescent waves [7]. The width of the PhC slab is $7\ \mu\text{m}$. The point source for the flat slab is realized by fabricating a $5\text{-}\mu\text{m}$ -wide waveguide tapered to $350\ \text{nm}$ and having $3\text{-}\mu\text{m}$ -wide trenches on both sides (see Fig. 2). For evanescent coupling of the source, a $500\ \text{nm}$ air-gap

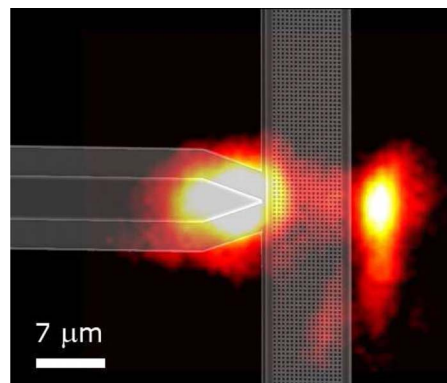


Fig. 2. (Color online) IR picture showing the point source, and the corresponding image formed by the flat lens for a source at wavelength $\lambda=1.51\ \mu\text{m}$. The IR image is overlaid on a scanning electron microscope image of the nanofabricated structure of flat lens and point source.

is created between the waveguide tip and the front edge of the PhC slab. The in-plane electromagnetic radiation into air is expected to converge and form an image at the far side of the flat lens.

In Fig. 2, the IR camera image shows the radiating point source in front of the PhC slab and the corresponding focused image formed $\approx 2.0\ \mu\text{m}$ away from the trailing edge of the flat lens. Here, the PhC images TE-polarized light and spatially disperses any small amount of TM-polarized light that may be radiated by the waveguide tip. The FWHM of the point source, from NSOM measurements [shown in Fig. 3(a)], is 1.4λ .

The PhC flat lens slab also supports surface waves [7] (if surface terminations are properly designed), which can enhance evanescent fields, thus leading to reconstruction of subwavelength details of an object at the image plane. From an effective medium approximation of the PhC [15], different surface terminations can be shown to lead to different excitations of surface modes.

For the lens shown in Fig. 3(a) the reconstruction of evanescent waves was not observed mainly due to the weak excitation of surface modes, and, on a minor note, because of the nonideal point source ($350\ \text{nm}$ -wide waveguide). We have optimized the design of the superlens to reflect subwavelength resolution enhancement by (i) modification of the surface terminations of the lens, thereby enhancing the excitation of surface modes, and (ii) by fabricating a waveguide tip that can approximate better the radiation field characteristics of an ideal point source (i.e., tapering the waveguide down to $50\ \text{nm}$). In design B [shown in Fig. 3(b)], we show that a cut through the middle of the air holes at the surface termination of the object plane leads to a focused spot size with FWHM of 1.0λ . For the optimized design C [shown in Fig. 3(c)], we removed the dielectric padding layers and terminated the lens surface by cutting through the middle of the air holes on both sides. Additionally, the waveguide was tapered down to $50\ \text{nm}$ to exhibit radiation field patterns that are closer (compared with the $350\ \text{nm}$ waveguide tip) to those of an ideal point source. The dramatic reduction in spot size from design A to design C is evident from Fig. 3.

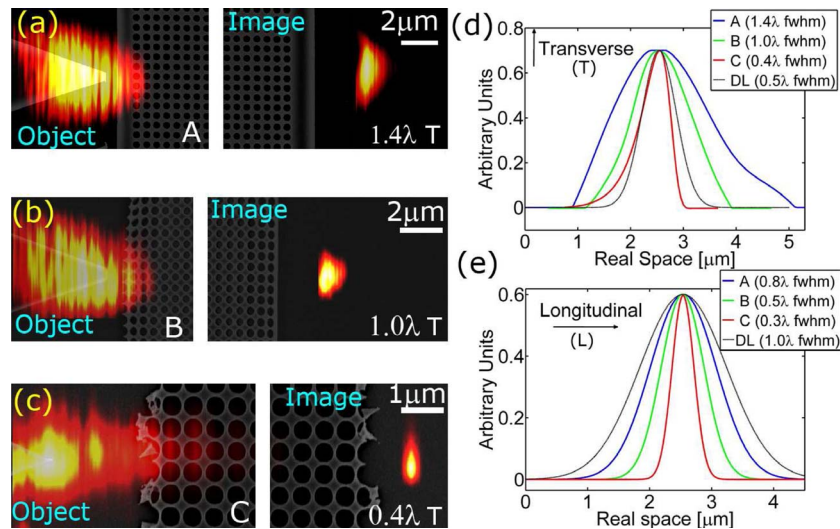


Fig. 3. (Color online) (a)–(c) show the SEM images of the various designs overlaid with the corresponding NSOM scans at $\lambda = 1.52 \mu\text{m}$ at the object and image planes. (a) Original design A with extra padding dielectric layers produced a focused spot of 1.4λ at FWHM. (b) Design B with a cut through the middle of the air holes at the surface termination of the object plane yielded a focused spot of 1.0λ . (c) Optimized design C with cuts through the middle of the air holes on both sides and waveguide tapered to 50 nm. The focused spot achieved by this design is 0.4λ . The spatial profile of the focused spot size in the (d) transverse (T) and (e) longitudinal (L) directions for the three designs are presented and compared with a theoretical diffraction limited (DL) profile ($\lambda/2$ for T and λ for L). Note that the NSOM images presented are raw data with a threshold applied to remove background noise.

The spatial profile of the focused spot size in the transverse (T) and longitudinal (L) directions for the three designs are presented and compared with a theoretical diffraction limited profile (DL) in Figs. 3(d) and 3(e), respectively. The spot size shrinks from 1.4λ (design A) to 0.4λ (design C). The spot area for the optimized design C ($0.12\lambda^2$) is four times smaller than the diffraction limited spot area $0.5\lambda^2$. This sub-wavelength image can be mapped by the NSOM only if reconstruction of evanescent waves takes place, along with the propagating waves required for focusing. The images contain some distortions, as observed from their asymmetric nature, since the evanescent components cannot be uniformly enhanced by the surface mode for all wave vectors [7].

In this Letter, we experimentally demonstrated negative refraction and flat lens imaging in InP/InGaAsP PhC nanostructures at $1.5 \mu\text{m}$ wavelength. The experimental negative-phase refractive index, calculated from the measured angle of refraction in the PhC prism experiment, is in excellent agreement with the one derived from band structure calculations. Also, the PhC flat lens imaging properties are consistent with the theory of generalized superlens imaging [16]. Most importantly, we have shown experimentally that the PhC lens is more than just a flat lens and that enhancement of evanescent fields (superlensing effect) can be engineered by appropriate truncation of the surface terminations of the lens. Subwavelength resolution of $0.12\lambda^2$ was achieved, which clearly overcomes Abbe's diffraction limit ($0.5\lambda^2$). This work comes closer than ever before to the realization of a true superlens in optics that recovers evanescent waves on top of the propagating waves required to achieve a real focus or image.

This work was supported by the Air Force Research Laboratories, Hanscom, through FA8718-06-

C-0045 and the National Science Foundation (NSF) through PHY-0457002. This work was performed in part at the Kostas Center for High-Rate Nanomanufacturing at Northeastern University and the Center for Nanoscale Systems, a member of the National Nanotechnology Infrastructure Network, under NSF Award ECS-0335765.

References

1. V. G. Veselago, *Sov. Phys. Usp.* **10**, 509 (1968).
2. J. B. Pendry, *Phys. Rev. Lett.* **85**, 3966 (2000).
3. V. M. Shalaev, *Nature Photon.* **1**, 41 (2007).
4. H. J. Lezec, J. A. Dionne, and H. A. Atwater, *Science* **316**, 430 (2007).
5. V. Podolskiy and E. Narimanov, *Opt. Lett.* **30**, 75 (2005).
6. M. Notomi, *Phys. Rev. B* **62**, 10696 (2000).
7. C. Luo, S. G. Johnson, J. D. Joannopoulos, and J. B. Pendry, *Phys. Rev. B* **68**, 045115 (2003).
8. A. Berrier, M. Mulot, M. Swillo, M. Qiu, L. Thylén, A. Talneau, and S. Anand, *Phys. Rev. Lett.* **93**, 073902 (2004).
9. E. Schonbrun, T. Yamashita, W. Park, and C. J. Summers, *Phys. Rev. B* **73**, 195117 (2006).
10. T. Matsumoto, K. S. Eom, and T. Baba, *Opt. Lett.* **31**, 2786 (2006).
11. Z. Lu, B. Miao, T. R. Hodson, C. Lin, J. A. Murakowski, and D. W. Prather, *Opt. Express* **15**, 1286 (2007).
12. R. Chatterjee, N. C. Panoiu, K. Liu, Z. Dios, M. B. Yu, M. T. Doan, L. J. Kaufman, R. M. Osgood, and C. W. Wong, *Phys. Rev. Lett.* **100**, 187401 (2008).
13. N. Fabre, L. Lalouat, B. Cluzel, X. Melique, D. Lippens, F. de Fornel, and O. Vanbesien, *Phys. Rev. Lett.* **101**, 073901 (2008).
14. N. Fang, H. Lee, C. Sun, and X. Zhang, *Science* **308**, 534 (2005).
15. T. Decoopman, G. Tayeb, S. Enoch, D. Maystre, and B. Gralak, *Phys. Rev. Lett.* **97**, 073905 (2006).
16. W. T. Lu and S. Sridhar, *Opt. Express* **13**, 10673 (2005).